

Preparation of FePd-RGO Bimetallic Composites with High Catalytic Activity for Formic Acid Electro-Oxidation

Nanting Li*

College of Materials Science and Engineering, Anhui University of Science & Technology, Huainan, Anhui 232001, China

FePd-RGO composites through the growth of uniformly dispersed iron-palladium bimetallic nanoparticles (NPs) on reduced graphene oxide (RGO) nanosheets were prepared by a two-step method. The firstly formed Fe is used as the seed for the subsequent Pd growth. The formation of Fe NPs on RGO in the first step is performed by an *in-situ* reduction reaction with the reducer ethylene glycol under oil bath at 180 °C. NPs in the as-prepared FePd-RGO have an average particle size of 6.5 nm, and Pd is added to one side of Fe which leads to the formation of Fe-Pd bimetallic interfaces. As compared with the commercial Pd black at the same loading, the composites have higher electro-catalytic activity, better electrochemical stability and higher resistance to CO poisoning for formic acid electro-oxidation.

Keywords graphene, bimetallic nanoparticles, microstructure, formic acid electro-oxidation

Introduction

Direct formic acid fuel cells (DFAFCs)^[1-4] can directly convert the chemical energy of formic acid into electricity, and they are expected to be the first energy conversion devices for commercial applications of powering portable electronics due to the high energy density.^[5-9] Formic acid oxidation reaction (FAOR) catalyzed by palladium (Pd) at the anode is one of the most important reactions in DFAFCs. However, Pd is a kind of noble metal, making that the cost of fuel cells is very high, and the electro-catalytic activity and stability of metallic Pd still can not meet the requirement of the commercialization.^[10] Especially, CO poisoning and aggregation/growth of Pd nanoparticles (NPs) can rapidly degrade the performance of DFAFCs.^[11] It has been reported that a conductive support material can play a role in altering the geometry and electronic characteristic of catalyst particles dispersed in the system.^[12,13] Thus, researchers have a strong motivation of dispersing Pd catalysts as small particles on a support material to increase their utilization.

Graphene is a novel two-dimensional one-atom-thick graphitic carbon system, which has attracted great attention as an electro-catalyst support due to its extremely high specific surface area ($2600\text{ m}^2\cdot\text{g}^{-1}$),^[14] good electrical conductivity^[15] and chemical stability.^[16-19] Yang *et al.*^[20] have synthesized Pd NPs with controllable morphology on the surface of reduced graphene oxide (RGO) by a novel procedure with palladium acetyl-

acetone [Pd(acac)₂] and poly(vinylpyrrolidone) (PVP) in the *N*-methylpyrrolidone (NMP) solution, and the cubic Pd/RGO catalyst shows a significantly high electro-catalytic ability in the FAOR. However, fabricating active electro-catalysts with lower noble metal loading is essential for the DFAFCs' development,^[21] and researchers have developed techniques for designing special nanostructures with a second element in order to achieve the high catalytic activity,^[22,23] stability and high utilization^[24] of Pd-based catalysts. For example, recently we have synthesized bimetallic core-shell structured Au@Pd NPs on graphene nanosheets by a simple one-step thermal reducing method.^[25] In comparison, Pd-based bimetallic catalysts (Pd—M, M=Fe, Co, Cu, Ni, Cr, etc.)^[26-31] with a noble metal and a transition base metal have more merits for the full use of the noble metal.

Herein, we report that reduced graphene oxide nanosheets supported uniformly dispersed Fe-Pd bimetallic NPs (FePd-RGO composites) are prepared by a two-step method. The composite's morphology, microstructure, size and composition are characterized by transmission electron microscopy (TEM), selected area electron diffraction (SAED), X-ray photoelectron spectroscopy (XPS) and X-ray diffraction (XRD), and the involved formation mechanism is proposed. Based on cyclic voltammetry, chronoamperometry, etc., we have also investigated the electro-catalytic performance and possible origin of the high activity and stability for the FAOR in alkaline electrolyte.

* E-mail: lamlinanting@163.com

Received July 13, 2016; accepted September 12, 2016; published online October 24, 2016.

Experimental

Materials and synthesis

Natural graphite powder (spectrum pure), H₂SO₄ (98 wt%, A.R.), KMnO₄ (A.R.), H₂O₂ (30 wt%, A.R.), HCl (36—38 wt%, A.R.), NaOH (A.R.), BaCl₂ (C.P.), HCOOH (A.R.) and anhydrous ethanol were all purchased from Sinopharm (Group) Shanghai Chemical Reagent Co. FeSO₄•7H₂O was obtained from Sinopharm Chemical Reagent Co. Ltd. Pd(NO₃)₂ was purchased from Nanjing Ning-Shi Chemical Reagent Co. Ltd, and ethylene glycol (EG) was obtained from Shanghai Jiu-Yi Chemical Reagent Co. Ltd. Commercial Pd black catalyst was purchased from Sigma-Aldrich Co. LLC. All reagents were used as received without further purification. Deionized water with a resistivity of exceeding 18.0 MΩ•cm from a JL-RO 100 Millipore-Q Plus water purifier was used throughout the experiments.

Graphite oxide was synthesized from natural graphite powder using the modified Hummers' method,^[32] and a typical synthesis refers to the reference.^[28] Fe-RGO and FePd-RGO composites can also be synthesized using our previously reported two-step method.^[28] In the first step, using EG as a reducing, stabilizing and dispersing agent, 31.4 mg of graphite oxide dispersed in 50 mL of EG was sonicated for 20 min, and then the pH of the entire solution was adjusted to 10 by adding NaOH (1.0 mol/L) followed by adding 81.4 mg FeSO₄•7H₂O under vigorous stirring in the oil bath at 180 °C for 0.5 h. After the solution was cooled to room temperature, the product (Fe-RGO) was washed and centrifuged several times by deionized water to remove the excess EG, then dried at 40 °C in a vacuum oven. In the second step, typically, 15 mL of 12.7 mmol/L Pd(NO₃)₂ and 7 mg Fe-RGO were dispersed in a beaker with 50 mL deionized water. The resulting solution was uniformly dispersed by sonication for 10 min, then vigorously stirred for 24 h at room temperature. The black product (FePd-RGO) was washed and centrifuged several times with deionized water, and finally dried in a vacuum oven at 40 °C.

Characterizations

TEM, HRTEM images and SAED patterns were obtained on a JEOL JEM-2100 TEM operating at 200 kV. XPS was measured on a Thermo Fisher K-alpha X-ray photoelectron spectrometer. Binding energies were determined with reference to carbon's C1s=284.6 eV. The products' composition and crystallographic properties were analyzed by XRD on a Rigaku Ultima III diffractometer (using Cu K α =1.5418 Å radiation) at a scanning rate of 5 (°)•min⁻¹ in the range of 20°—90°.

Electrode preparation and electrochemical measurements

5.7 mg commercial Pd black and 5.0 mg FePd-RGO were dispersed in 250 μL anhydrous ethanol and 250 μL

Nafion (Sigma-Aldrich, USA) under ultrasonic agitation to form the electro-catalyst ink, respectively. The electro-catalyst ink (15 μL) was then deposited on the surface of a glassy carbon electrode (GCE, geometric area =0.1256 cm²) and dried at room temperature.

Electrochemical measurements were performed by a CHI 660D electrochemical analyzer (CH Instruments, Inc., Shanghai) with a conventional three-electrode cell including GCE, saturated calomel electrode (SCE) and platinum foil, and the potentials were measured with SCE as the reference.

Results and Discussion

TEM observation

Figure 1a shows the TEM image of Fe-RGO composites, and iron gathers together to form unevenly dispersed aggregates on the RGO surface due to the cause of the preparation process and the nature of Fe NPs. Inset 1a is the corresponding SAED pattern, which confirms the completely amorphous nature of aggregates. Figure 1b is the TEM image of as-prepared FePd-RGO composites, showing that the composites have highly dispersed Fe-Pd NPs with the narrow size distribution on the RGO surface, and a continuous sonication for 2 min before TEM characterization does not remove NPs from the RGO surface, indicating a strong interaction between them. Inset 1b is the corresponding local magnified image, which shows that the supported NPs have the irregular shape with less smooth edges. The HRTEM image of Figure 1c indicates that Fe and Pd elements co-exist on the RGO surface and NPs with an average 6.5 nm size have Fe-Pd bimetallic interfaces with multiple orientations of lattice fringes. Due to that the (111) plane of face-centered cubic (fcc) Pd and the (110) plane of cubic (bcc) α-Fe have a *d*-spacing of 0.22 nm (JCPDS No. 46-1043)^[33] and 0.20 nm (JCPDS No. 06-0696),^[34] respectively, the measured *d*-spacing between the two nearest atom rows is 0.19 nm, and this

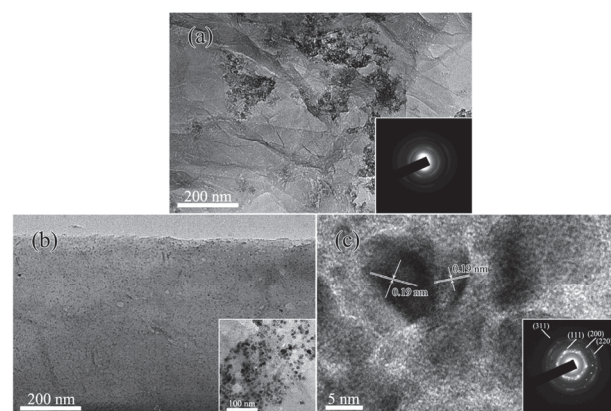


Figure 1 (a) TEM image of Fe-RGO; (b) TEM image of FePd-RGO with the corresponding local magnified image, and (c) HRTEM image of (b). Insets (a) and (c) are the corresponding SAED patterns, respectively.

result indicates that Fe and Pd elements have a much larger mismatch degree, leading to the existence of the lattice contraction effect in bimetallic NPs which have a much larger strain. Lattice contraction effect illustrates that lattices of metal Fe and Pd do not exist independently but are interlaced with each other, which also evidences that Fe in the first step can act as the seed for the formation and subsequent growth of Pd. Inset 1c is the corresponding SAED pattern of Fe-Pd NPs, and the diffraction rings are indexed to the (111), (200), (220) and (311) crystal planes for fcc Pd on the outer layer of NPs, confirming the polycrystalline nature.

XPS patterns

Figure 2a shows XPS patterns of GO and FePd-RGO before and after the reduction. The bands at 284.8 and 531.0 eV are associated with C1s and O1s, respectively, and as compared with GO, oxygen-containing functional groups of RGO are partially removed after the reduction. Two weak peaks (Figure 2b) at binding energies of 711.1 and 724.8 eV can be assigned to the metallic

Fe2p_{3/2} and Fe2p_{1/2}, respectively,^[35] and one strong peak (Figure 2c) at 334.9 eV corresponds to the Pd3d. These results indicate that Fe and Pd are present as elements in FePd-RGO rather than oxygen-containing compounds. The PdO₂ peak at 337.3 eV in Figure 2c may be caused by the surface oxidation and/or chemisorption of environmental oxygen during the preparation process. By calculating the peak area, the Pd and Fe contents are 2.19 wt% and 0.22 wt%, respectively.

XRD patterns

Crystal structures of FePd-RGO composites and graphite oxide are characterized by XRD, as shown in Figure 3. The FePd-RGO shows a wide peak of the C (002) plane at $2\theta=24^\circ$ (red curve), confirming that the conjugated graphene network (sp^2 C) of RGO nanosheets has been re-established after the partial reduction. The XRD pattern also reveals that Fe-Pd NPs have two weak Fe peaks at $2\theta=44.7^\circ$ and 65.0° in good agreement with cubic (bcc) α -Fe (110) and (200) planes (JCPDS No. 06-0696),^[34] respectively. Moreover, in addition to Fe diffraction peaks, five peaks at $2\theta=40.1^\circ$, 46.7° , 68.1° , 82.1° and 86.6° correspond to Pd (111), (200), (220), (311) and (222) crystal planes, respectively.^[33] The particle size of bimetallic Fe-Pd NPs is estimated by Scherrer's equation from Pd (111), (200) and (220) primary crystal plane parameters, and averaged as 6.5 nm which is very close to the TEM result.

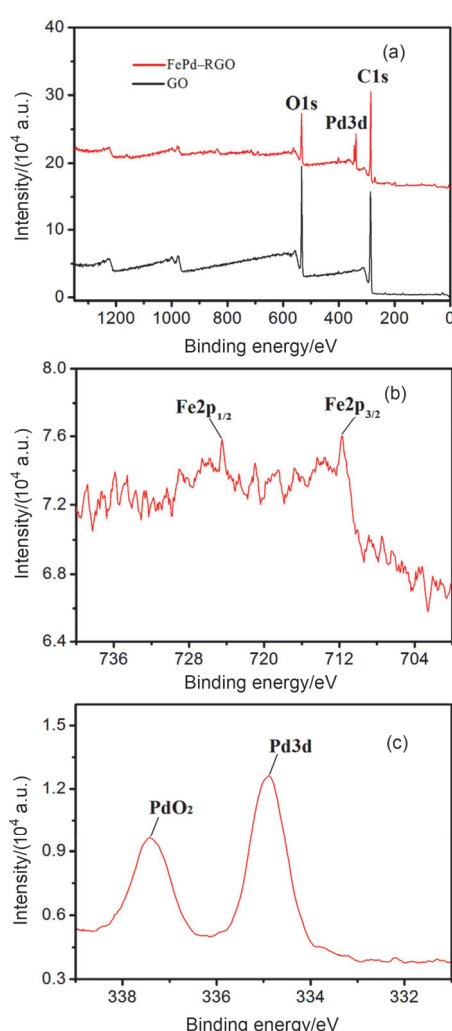


Figure 2 XPS patterns of GO and FePd-RGO (a), Fe2p (b) and Pd3d (c).

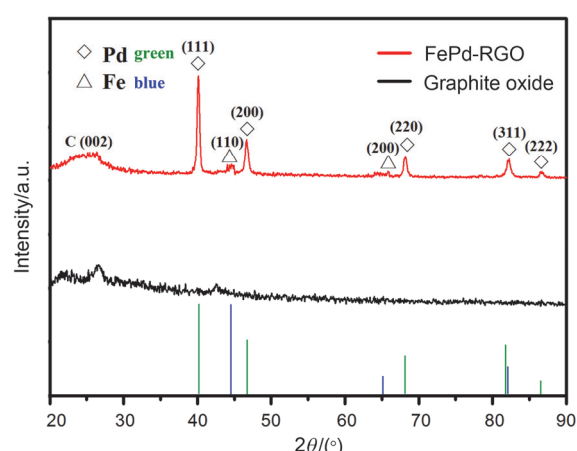


Figure 3 XRD patterns of graphite oxide (black) and FePd-RGO (red) with the standard peaks of Fe and Pd added.

The formation mechanism for Fe-Pd NPs supported on RGO can refer to the related content of our previous paper,^[28] which is demonstrated as follows: in the first step, as compared with the bare graphene surface, residual functional groups such as COOH, OH, etc., on the RGO surface have stronger attraction toward metal ions, thus acting as metal-anchoring sites to facilitate the formation of Fe nuclei with good stability by chemisorption and physisorption. The formed Fe is used as the seed for the subsequent Pd growth, and preferentially starts to reduce Pd^{2+} to obtain Pd added to one side of Fe on the RGO surface, thus forming Fe-Pd NPs with

bimetallic interfaces. Fe-Pd NPs with bimetallic interfaces have the formation of the modified electronic structure of Fe decorated Pd NPs, and these electrons in metals can interact with existing free electrons on the surface of graphene, leading to the existence of the electric synergistic effect between metals and graphene. The overall result is the enhancement of the electrochemical activity and stability of FePd-RGO.

Electrochemical studies on FePd-RGO for HCOOH oxidation

Figure 4 shows CVs of commercial Pd black (red) and FePd-RGO (blue) modified electrodes in 200 mL mixed solution containing 0.5 mol/L NaOH and 0.5 mol/L HCOOH at a scan rate of 50 mV•s⁻¹. Weak oxidation current is observed on the commercial Pd black modified electrode, while the FePd-RGO modified electrode has much stronger oxidation currents in the forward and reverse scan. As can be seen from Figure 4, there is a weak wide formic acid oxidation peak at about 0.13 V, and the oxidation current is 4×10^{-5} A. The CV area of FePd-RGO is apparently much larger than that of commercial Pd black, indicating that the FePd-RGO composites have better catalytic activity for HCOOH electro-oxidation. Firstly, the Pd sites in bimetallic interfaces are responsible for formic acid electro-oxidation to form adsorbed carbon monoxide (CO_{ads}), which poisons the catalyst surface against the further oxidation, while the Fe sites provide adsorbed hydroxyl groups (OH_{ads}), which are in favor of the oxidant for the removal of CO_{ads}. Secondly, due to the interaction between Fe and Pd, such as the electronic effect, the presence of Fe changes the electronic structure of Pd in a way that it lowers the CO adsorption energy,^[30] and Pd can simultaneously improve the catalytic performance by establishing a good conductive network on the RGO surface, thus facilitating charge-transfer and mass-transfer processes. These results reveal that Fe has a synergistic effect on the Pd catalyst and uniformly dispersed Fe-Pd NPs with bimetallic interfaces provide more active atoms, making Fe-Pd NPs electrochemically more accessible for reactants and improving the activity of FePd-RGO and the output when used in fuel cells.

Researchers have widely applied chronoamperometry to explore high durability, long-term electro-catalytic activity and stability of fuel cells.^[36-38] Figure 5 shows current-time curves of commercial Pd black (red) and FePd-RGO (blue) modified electrodes in 200 mL mixed solution containing 0.5 mol/L NaOH and 0.5 mol/L HCOOH. Under a fixed potential of 1.2 V, an initial fast current decay has been displayed, followed by a slower attenuation in both electrodes that gradually reaches a pseudo-steady state, which is due to the initially adsorbed intermediate species being depleted to an equilibrium level. As compared with commercial Pd black, the FePd-RGO modified electrode exhibits 5.5 times higher initial current and the current of FePd-RGO

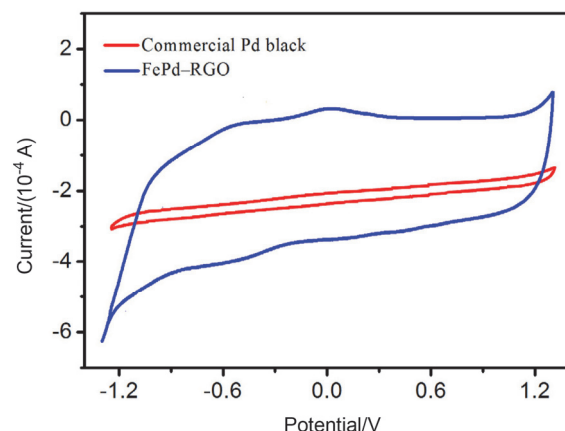


Figure 4 CVs of commercial Pd black (red) and FePd-RGO (blue) modified electrodes in 200 mL mixed solution containing 0.5 mol/L NaOH and 0.5 mol/L HCOOH at a scan rate of 50 mV•s⁻¹.

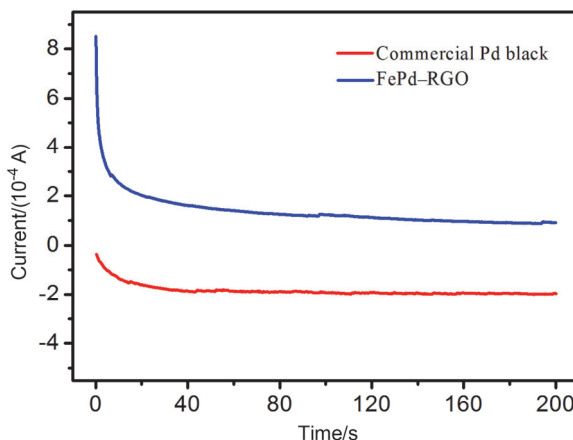


Figure 5 Current-time curves of commercial Pd black (red) and FePd-RGO (blue) modified electrodes in 200 mL mixed solution containing 0.5 mol/L NaOH and 0.5 mol/L HCOOH.

maintains a higher steady state during the whole measurement. This can be attributed to that the intrinsically electronic structure of RGO and the stable nanostructure with bimetallic interfaces have been preserved in FePd-RGO. The slower decay of the steady-state current in FePd-RGO suggests that the electrode surface does not experience deactivation during the electro-oxidation process and the FePd-RGO modified electrode has a better tolerance towards the CO-like poisoning.

Figure 6 shows open circuit voltage (OCV)-time curves of commercial Pd black (red) and FePd-RGO (blue) modified electrodes for 200 s. The value of OCV illustrates the extent of CO-like poisoning, and the larger the value, the more serious the poisoning. Obviously, the FePd-RGO electrode exhibits more stable and lower voltage with a low polarization loss than the commercial Pd black electrode, which is attributed to that a good conductive network with lower internal resistance has formed between Fe and Pd, which facilitates more complete oxidation of HCOOH to CO₂ with less carbona-

ceous accumulation.^[39-43]

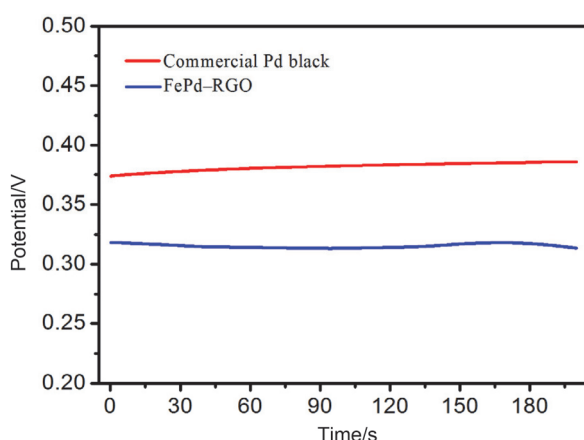


Figure 6 OCV-time curves of commercial Pd black (red) and FePd-RGO (blue) modified electrodes in 200 mL mixed solution containing 0.5 mol/L NaOH and 0.5 mol/L HCOOH.

Electrochemical impedance spectroscopy (EIS) is a powerful tool which characterizes electrode surface interactions and ion diffusion kinetic features.^[44,45] Figure 7 shows Nyquist plots for commercial Pd black (red) and FePd-RGO (blue) modified electrodes in 200 mL mixed solution containing 0.5 mol/L NaOH and 0.5 mol/L HCOOH. Based on the equivalent electric circuit as shown in the inset, the charge transfer resistance (R_{ct}) can be estimated from the analysis of EIS, where R_s is the uncompensated solution resistance between the reference electrode and the working electrode and Q is used for constant phase elements instead of capacitances. The values of the charge transfer resistance R_{ct} (derived from the amplitude of the plot semicircles and accounting for the kinetics of the electronic transfer) can be calculated by fitting the experimental data using ZsimpWin software based on the equivalent circuit shown in the inset of Figure 7. The R_{ct} values for commercial Pd black and FePd-RGO are 104.1 and 52.6 $\Omega \cdot \text{cm}^2$, respectively. It is clear from Figure 7 that the curve of the commercial Pd black electrode is more vertical than that of the FePd-RGO electrode in the low frequency region, and the value order of R_{ct} estimated from the equivalent electric circuit is $R_{ct}(\text{FePd-RGO/GCE}) < R_{ct}(\text{commercial Pd black/GCE})$, indicating that the commercial Pd black electrode with a more vertical curve has a larger R_{ct} value. This result also demonstrates that the electron transfer rate on FePd-RGO is faster than that on commercial Pd black, which is consistent with the higher catalytic activity of FePd-RGO. While the commercial Pd black electrode has a larger semicircle than the FePd-RGO electrode (with an oblique line) in the high frequency region (inset), indicating that the commercial Pd black electrode has a larger R_s . These results are in agreement with the CVs data (Figure 4), confirming that the FePd-RGO composites with bimetallic interfaces have better conductivity.

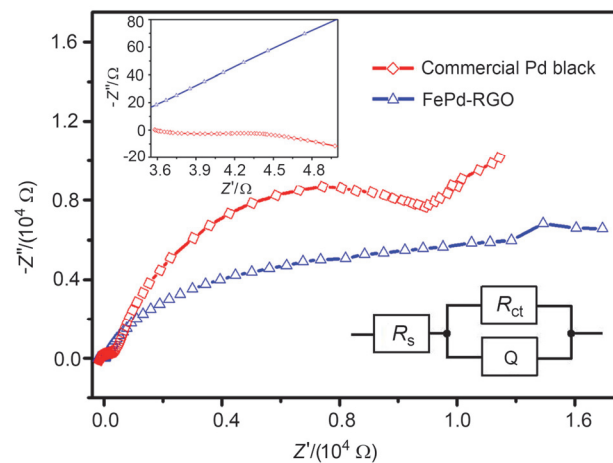


Figure 7 Nyquist plots of commercial Pd black (red) and FePd-RGO (blue) modified electrodes in 200 mL mixed solution containing 0.5 mol/L NaOH and 0.5 mol/L HCOOH. Insets show the magnified high-frequency region and the equivalent electric circuit.

Conclusions

In summary, RGO supported uniformly dispersed Fe-Pd NPs with an average particle size of 6.5 nm are prepared by a two-step method, where the firstly formed Fe is used as the seed for the subsequent Pd growth and Pd is added to one side of Fe, thus forming Fe-Pd bimetallic interfaces. The composites' morphology, microstructure, size and composition have been characterized, and the involved formation mechanism is proposed. The FePd-RGO composites are used as an electro-catalyst for the HCOOH oxidation in alkaline electrolyte and the catalytic performance has been investigated. As compared with the commercial Pd black at the same loading, the FePd-RGO composites have higher electro-catalytic activity, better electrochemical stability and higher resistance to CO poisoning. The advantage and innovation of our method are fast reaction speed, short required time and good products' reproducibility, and it will be used to synthesize other metals/RGO composites for energy-related field applications, *i.e.*, supercapacitors, photocatalysts, solar cells, *etc.*

Acknowledgement

This work was supported by the PAPD, the Fundamental Research Funds for the Central Universities, the Innovation Fund of Jiangsu Province, the Natural Science Foundation of Jiangsu Province, the National Natural Science Foundation of China, and the State Key Program for Basic Research of China.

References

- [1] Wang, K. Q.; Wang, B.; Chang, J. F.; Feng, L. G.; Xing, W. *Electrochim. Acta* **2014**, *150*, 329.
- [2] Zhao, Y.; Qin, S. J.; Li, Y.; Deng, F. X.; Liu, Y. Q.; Pan, G. B. *Elec-*

- trochim. Acta* **2014**, *145*, 148.
- [3] Chang, J. F.; Feng, L. G.; Liu, C. P.; Xing, W.; Hu, X. L. *Angew. Chem., Int. Ed.* **2014**, *53*, 122.
- [4] Moreno-Zuria, A.; Dector, A.; Cuevas-Muñiz, F. M.; Esquivel, J. P.; Sabaté, N.; Ledesma-García, J.; Arriaga, L. G.; Chávez-Ramírez, A. U. *J. Power Sources* **2014**, *269*, 783.
- [5] Chang, J. F.; Li, S. T.; Feng, L. G.; Qin, X. J.; Shao, G. J. *J. Power Sources* **2014**, *266*, 481.
- [6] Li, N. T.; Tang, S. C.; Pan, Y.; Meng, X. K. *Mater. Res. Bull.* **2014**, *49*, 119.
- [7] Zhang, J. F.; Xu, Y.; Zhang, B. *Chem. Commun.* **2014**, *50*, 13451.
- [8] Barakat, N. A. M.; Abdelkareem, M. A.; Shin, G.; Kim, H. Y. *Int. J. Hydrogen Energ.* **2013**, *38*, 7438.
- [9] Rejal, S. Z.; Masdar, M. S.; Kamarudin, S. K. *Int. J. Hydrogen Energ.* **2014**, *39*, 10267.
- [10] Zhang, L. Y.; Guo, C. X.; Pang, H. C.; Hu, W. H.; Qiao, Y.; Li, C. M. *ChemElectroChem* **2014**, *1*, 72.
- [11] Ren, M. J.; Zou, L. L.; Yuan, T.; Huang, Q. H.; Zou, Z. Q.; Li, X. M.; Yang, H. *J. Power Sources* **2014**, *267*, 527.
- [12] Zhao, H. R.; Wang, Y.; Tang, Q. H.; Wang, L.; Zhang, H.; Quan, C.; Qi, T. *Int. J. Hydrogen Energ.* **2014**, *39*, 9621.
- [13] Qu, W. L.; Gu, D. M.; Wang, Z. B.; Zhang, J. *J. Electrochim. Acta* **2014**, *137*, 676.
- [14] Li, X.; Chen, Y.; Cheng, Z. D.; Jia, L. S.; Mo, S. P.; Liu, Z. W. *Appl. Energ.* **2014**, *130*, 824.
- [15] Chen, G. Q.; Liu, Y. X.; Liu, F.; Zhang, X. *Appl. Surf. Sci.* **2014**, *311*, 808.
- [16] Zhou, S.; Bongiorno, A. *Sci. Rep.* **2013**, *3*, 2484.
- [17] Hu, H. X.; Hu, Z. A.; Ren, X. Y.; Yang, Y. Y.; Qiang, R. B.; An, N.; Wu, H. Y. *Chin. J. Chem.* **2015**, *33*, 199.
- [18] Shi, M. Q.; Zhao, D.; Liu, W. M.; Chu, Y. Q.; Ma, C. A. *Chin. J. Chem.* **2014**, *32*, 233.
- [19] Guo, R. H.; Wu, W. H. *Gen. Chem.* **2016**, *2*, 66.
- [20] Yang, S. D.; Shen, C. M.; Tian, Y.; Zhang, X. G.; Gao, H. J. *Nanoscale* **2014**, *6*, 13154.
- [21] Shen, L. P.; Li, H. Z.; Lu, L.; Luo, Y. F.; Tang, Y. W.; Chen, Y.; Lu, T. H. *Electrochim. Acta* **2013**, *89*, 497.
- [22] Kakaei, K.; Dorraji, M. *Electrochim. Acta* **2014**, *143*, 207.
- [23] Dong, Q.; Zhao, Y.; Han, X.; Wang, Y.; Liu, M. C.; Li, Y. *Int. J. Hydrogen Energ.* **2014**, *39*, 14669.
- [24] Matin, M. A.; Jang, J. H.; Kwon, Y. U. *J. Power Sources* **2014**, *262*, 356.
- [25] Li, N. T.; Tang, S. C.; Meng, X. K. *J. Mater. Sci. Technol.* **2014**, *30*, 1071.
- [26] Sun, J. M.; Karim, A. M.; Zhang, H.; Kovarik, L.; Li, X. H. S.; Hensley, A. J.; McEwen, J. S.; Wang, Y. *J. Catal.* **2013**, *306*, 47.
- [27] Wang, Y.; Zhao, Y.; Yin, J.; Liu, M. C.; Dong, Q.; Su, Y. Q. *Int. J. Hydrogen Energ.* **2014**, *39*, 1325.
- [28] Li, N. T.; Tang, S. C.; Meng, X. K. *J. Mater. Sci. Technol.* **2015**, *31*, 30.
- [29] Ren, M. J.; Zhou, Y.; Tao, F. F.; Zou, Z. Q.; Akins, D. L.; Yang, H. J. *Phys. Chem. C* **2014**, *118*, 12669.
- [30] Yang, H. J.; Wang, H.; Li, H.; Ji, S.; Davids, M. W.; Wang, R. F. *J. Power Sources* **2014**, *260*, 12.
- [31] Wen, W. J.; Li, C. Y.; Li, W. P.; Tian, Y. *Electrochim. Acta* **2013**, *109*, 201.
- [32] Hummers, W. S.; Offeman, R. E. *J. Am. Chem. Soc.* **1958**, *80*, 1339.
- [33] Zhang, Z. Q.; Huang, J. L.; Zhang, L.; Sun, M.; Wang, Y. C.; Lin, Y.; Zeng, J. *Nanotechnology* **2014**, *25*, 435602.
- [34] Zhang, Q. Y.; Li, B.; Ma, Z.; Wang, Y. G.; Li, X. *J. Alloy Compd.* **2014**, *617*, 713.
- [35] Han, W. L.; Tang, Z. C.; Zhang, P.; Lu, G. X. *RSC Adv.* **2014**, *4*, 23262.
- [36] Yang, G. X.; Li, Y.; Yuan, Z. H.; Kong, X. Y.; Li, T.; Chen, G. Y.; Lu, T. H.; Sun, Y. M. *J. Fuel Chem. Technol.* **2013**, *41*, 1367.
- [37] Tsujiguchi, T.; Hirano, S.; Iwakami, T.; Nakagawa, N. *J. Power Sources* **2013**, *223*, 42.
- [38] Cai, W. W.; Liang, L.; Zhang, Y. W.; Xing, W.; Liu, C. P. *Int. J. Hydrogen Energ.* **2013**, *38*, 212.
- [39] Podlovchenko, B. I.; Maksimov, Y. M. *Mendeleev Commun.* **2013**, *23*, 157.
- [40] Zhai, C. Y.; Zhu, M. S.; Bin, D.; Wang, H. W.; Du, Y. K.; Wang, C. Y.; Yang, P. *ACS Appl. Mater. Interfaces* **2014**, *6*, 17753.
- [41] Ren, F. F.; Wang, H. W.; Zhai, C. Y.; Zhu, M. S.; Yue, R. R.; Du, Y. K.; Yang, P.; Xu, J. K.; Lu, W. S. *ACS Appl. Mater. Interfaces* **2014**, *6*, 3607.
- [42] Ren, F. F.; Zhai, C. Y.; Zhu, M. S.; Wang, C. Q.; Wang, H. W.; Bin, D.; Guo, J.; Yang, P.; Du, Y. K. *Electrochim. Acta* **2015**, *153*, 175.
- [43] Zhai, C. Y.; Zhu, M. S.; Pang, F. Z.; Bin, D.; Lu, C.; Goh, M. C.; Yang, P.; Du, Y. K. *ACS Appl. Mater. Interfaces* **2016**, *8*, 5972.
- [44] Cui, X.; Wu, S. N.; Jungwirth, S.; Chen, Z. B.; Wang, Z. H.; Wang, L.; Li, Y. X. *Nanotechnology* **2013**, *24*, 295402.
- [45] Qu, W. L.; Wang, Z. B.; Sui, X. L.; Gu, D. M. *Int. J. Hydrogen Energ.* **2014**, *39*, 5678.

(Zhao, X.)